Paper: ASAT-14-228-AE

14th International Conference on
AEROSPACE SCIENCES & AVIATION TECHNOLOGY,
ASAT - 14 – May 24 - 26, 2011, Email: asat@mtc.edu.eg
Military Technical College, Kobry Elkobbah, Cairo, Egypt
Tel: +(202) 24025292 –24036138, Fax: +(202) 22621908

Surrogate-Based Multi-Objective Aerothermodynamic Design Optimization of Hypersonic Spiked Bodies

M. Y. M. Ahmed* and N. Qin†

Abstract: Aerospikes can reduce both drag and aeroheating for hypersonic vehicles with blunt forebodies. However, the performance of the spike depends largely upon its design and the forebody geometry. Balancing the design for drag and aeroheating reduction can be competing. For some design combinations, the flow can be unstable which invokes undesirable consequence. In this work, a stability-constrained bi-objective design optimization for the hypersonic spiked bodies was conducted. The multi-objective algorithm was coupled with the Kriging surrogates that were constructed based on numerical solutions of laminar viscous flows around the geometries.

Nomenclature

$\mathbf{A}$	=	Vandermonde matrix of training samples
B	=	Length of the cylindrical part of the forbody
D	=	Forebody diameter
L	=	Forebody length
L_d	=	Aerodisk length
L_S	=	Spike length
M	=	Mach number
P	=	Pressure
p	=	Correlation exponent
$\mathbf{R}$	=	Correlation matrix
R	=	Forebody radius
$\mathbf{r}$	=	Correlation vector
r	=	Forebody nose radius
r_d	=	Aerodisk base radius
r_n	=	Aerodisk nose radius
Re	=	Reynolds number
$\mathbf{y}$	=	Vector of high fidelity responses
y	=	High fidelity response
$\hat{y}$	=	Surrogate response
β	=	Mean of Kriging surrogate
μ	=	Dynamic viscosity
θ	=	Correlation parameter
ρ	=	Density

* Egyptian armed forces, Egypt.
† Professor of Aerodynamics, Department of Mechanical Engineering, University of Sheffield, UK, Associate Fellow AIAA.

Subscripts

∞ = Freestream value
D = Referred to the forebody diameter

I. Introduction

AMONG various design requirements, reducing both drag and aerodynamic heating is the most crucial in the design of hypersonic vehicles. On one hand, reducing the aerodynamic drag enables reaching the desired range, economizing the fuel usage, simplifying the propulsion system requirements, and maximizing the ratio of payload to take-off gross weight [1]. On the other hand, high levels of aerodynamic heating can cause malfunction [2] or even damage of the delicate on-board equipments [3, 4]. In addition, excessive heating can cause ablation to the vehicle surface material which yields fluctuations in the vehicle performance [5]. In the presence of high pressure loads, severe heating can cause a complete material failure [6]. Employing the conventional thermal protection shields adds to the weight of the vehicle and the complexity of its design [7]. Nonetheless, communication black-out caused by the ionized air associated with elevated temperatures cannot to be solved by the thermal protection shields.

Pointed slender bodies generate lower drag compared with blunt bodies at hypersonic conditions. Hence, they provide a good choice as far as drag reduction is concerned. On the other hand, blunt bodies were found to yield lower heating levels compared with their pointed counterparts [1, 8-10]. In fact, blunting the body is viewed as the primary design option in hypersonic regimes [11]. Moreover, in some practical applications, blunting the body nose becomes a favoured design requirement on its own [2,12-15]. In fact, hypersonic vehicles such as missiles, interplanetary space missions, space planes, and launch missiles usually have blunt shapes [10, 16]. The design of the re-entry vehicles such as reusable launch vehicles, long-range and ballistic missiles is rather complicated. On one hand, it is desired to use a pointed slender geometry to minimize the drag during the take-off (ascent) phase. On the other hand, a blunt design is advantageous during the descent phase to reduce the excessive aeroheating levels during re-entry and to generate the desired vehicle deceleration [1,9,10,17]. Obviously, designing a vehicle that simultaneously satisfies both minimum drag and aerodynamic heating is not straightforward and there is a challenging trade-off between these two vital requirements.

However, it is believed that these two requirements can be met by altering the flowfield pattern around the blunt body so as to eliminate the strong detached bow shock wave. A variety of techniques have been implemented in this regard. These techniques include spikes and aerodisks, focused gas jet, laser or microwave beams upstream of the nose stagnation point, energy deposition using plasma torch, arc discharge, dc corona discharge, and even supersonic projectiles fired ahead of the blunt body [10]. Out of these varieties of techniques, the use of spikes proved to be the simplest and the most effective technique in reducing both drag and aerodynamic heating [14]. It was found as a compromise of two requirements namely, lower aerodynamic heating for re-entry and lower drag for atmospheric flights [18].

The spike is simply a slender cylindrical rod mounted at the stagnation point of the blunt body and projected in the upstream direction. The spike introduces two major modifications to the flowfield upstream of the blunt body. Firstly, it replaces the strong detached shock wave with a system of weaker oblique shock waves. Secondly, it acts as a "flow separator"; the spike encourages the separation of the boundary layer from its surface and the creation of a shear layer. The latter propagates downstream, reattaches on the blunt body surface, and envelopes a zone of recirculation in which the flow attains low pressure and velocity values. This zone screens a considerable portion of the blunt body surface and results in a significant drop in surface pressure and temperature. Only at the zone of shear layer reattachment on the blunt

body, the local heating rate and surface pressure attain high values. In addition, to turn the flow outside the shear layer parallel to the body surface, a shock wave is created at the reattachment zone; the reattachment shock. Immediately downstream of the reattachment shock, the flow pressure attains high local values. However, the overall effect is a significant reduction in both drag and the aerodynamic heating as compare to those without the spike.

To further enhance the effectiveness of the spike, a relatively larger tip, called the aerodisk, can be used. An aerodisk mounted at the tip of a spike of a fixed length has the role of providing further reduction in both drag [19] and aerodynamic heating [20] over a wider range of Mach numbers [6] and incidence angles [17]. It can also compensate the drag reduction in cases when a shorter spike is necessary for design [14]. The typical features of the flowfield associated with unspiked and aerodisk-spiked blunt bodies in high flow speeds are illustrated in Fig. 1.

However, under certain flight conditions and spiked vehicle configurations, the flow can become unstable which invokes some problems such as fluctuations in surface pressure and heat flux [22], elevated acoustic and structural dynamic loads [23], bending of the spike [15], and flight disturbances and control complications [24,25]. These problems can get worse due to the hysteresis phenomena taking place during the extension and retraction of protruding and telescopic spikes [23,26]. It is known that, the performance of spikes and the flow stability depend upon both the blunt body geometry and spike designs [27,28]. It is also proved that the spike's efficiency does not improve monotonically with the spike length [17,21,29-31] or the aerodisk size [20,32]. For more details about the physics of the flow around spiked bodies, the interested reader is advised to refer to the author's work in this respect [33].

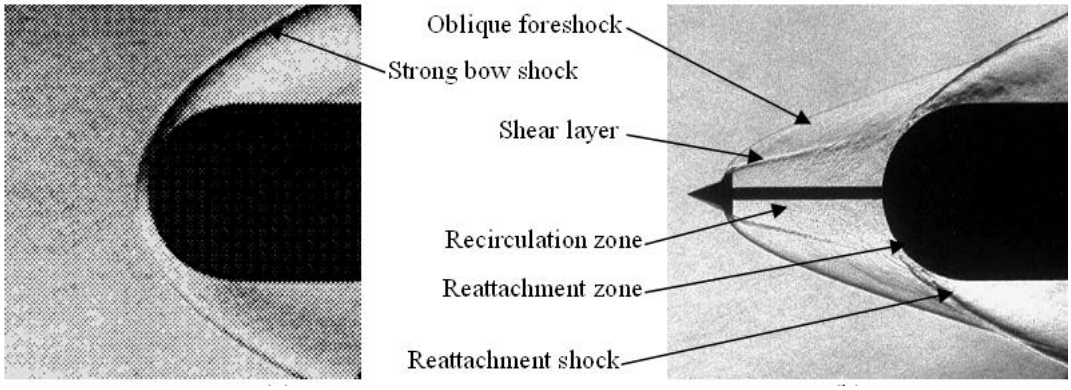

Figure 1 Macroscopic features of the flowfield ahead of a blunt body in hypersonic speeds (a) without [21], and (b) with the spike/ aerodisk [4]

The need to optimize the spiked blunt body design was explicitly highlighted in the literature [4,17,20,27,32,34]. However, a study dedicated to the design optimization of spiked blunt bodies in high speed regimes has not yet been found in the literature. The purpose of the present work is to conduct a design optimization study for the spiked blunt bodies. The optimization involves the design of the forebody, the spike length, and the aerodisk. This study is an extension of a previous study by the authors [35] in which the spike and aerodisk size were optimized while the forebody was a hemisphere of a fixed geometry. The optimization objectives are minimizing the drag and aeroheating on the spiked blunt body while keeping the flow stable.

The present work utilizes two of the state-of-the-art topics in the field of CFD-based aerodynamic design optimization (ADO), namely, surrogate modelling and multiobjective evolutionary optimization algorithms. In fact, the bottleneck in any CFD-based ADO application is that the use of CFD models as the analysis tool is extremely expensive, time consuming, and memory demanding. A surrogate is simply a cheaper alternative for CFD

model that is designed prior to optimization using minimum CFD runs. A sampling technique is used to select the sites in the design space in which the CFD model is implemented (training samples). Based on the high-fidelity CFD response at these samples, the surrogate is constructed, its accuracy is assessed (and, if required, improved), and finally coupled with the optimization algorithm in lieu of the CFD model.
Evolutionary, gradient-free, population-based optimization algorithms are known to overperform the traditional, gradient-based search methods. This is particularly evident in case if global optimum is desired or non-conventional designs are sought of. However, directly coupling these algorithms with the CFD model can be prohibitively expensive. The significantly lower cost of the surrogate model enables the use of evolutionary population-based optimization algorithms. To efficiently handle the multiple design objectives and to provide the designer/ decision maker with a variety of trade-off solutions, the evolutionary algorithms were further improved to the multiobjective evolutionary algorithms; MOEA.
In this work, one of the most powerful, flexible, and popular surrogates, Kriging, is coupled with one of the most efficient multiobjective algorithms, NSGA-II in order to find the optimal combinations of forebody shapes and spike designs. The remainder of this paper is arranged as follows. In the next section, the aspects of the techniques used in this study are illustrated including the flow CFD solver, the metamodel, and the multi-objective algorithm. Next, the main results of the optimization study are discussed. The paper finalizes with the main conclusions and recommendations for future work.

II. Methodology

A. Geometry representation and design parameterization

The proposed shape of the spiked blunt body is described as follows, as shown in Fig. 2:
The body: a blunt cone with a spherical nose,
The spike: a thin circular cylinder,
The aerodisk: a small blunt cone with a spherical nose

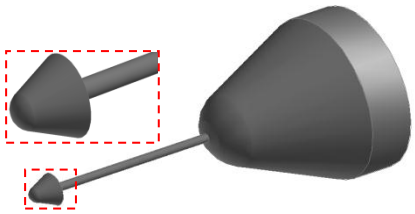

Figure 2 Geometric representation of a spiked blunt body with a close-up at the aerodisk

Next, the design parameters are specified. They are the set of *independent* geometric variables that *fully* describe the design and, in the same time, enable the generation of a wide variety of designs. The proposed design above has the following design variables:

Forebody: radius: R, length of the cylindrical part: B, length of the conical part: L, nose radius: r, cone semi-apex angle: θ_b,
Spike: length: L_S, radius: r_S
Aerodisk: radius: r_d, length of the conical part: L_d, nose radius: r_n, cone semi-apex angle: θ_d.

These eleven design variables are illustrated in Fig. 3.

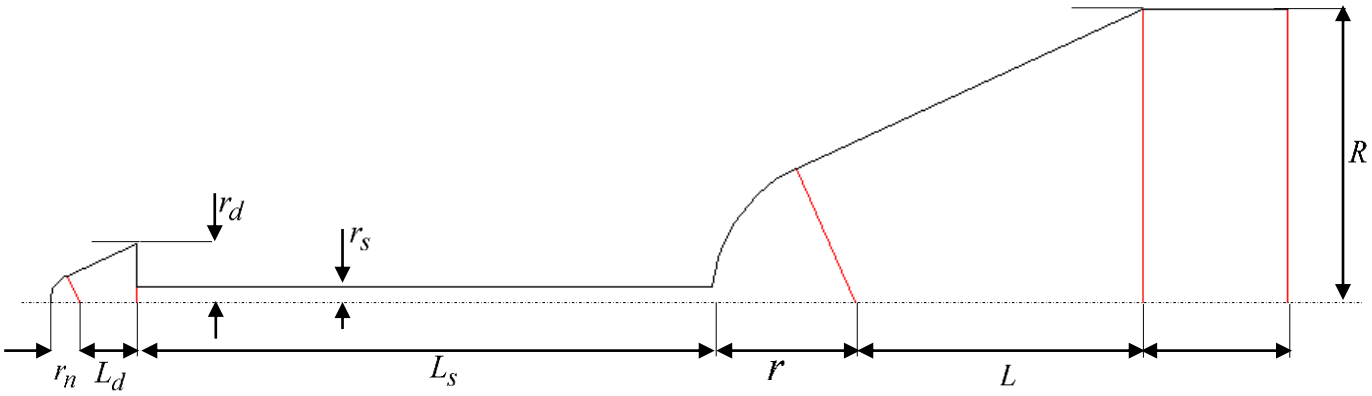

Figure 3 Design variables of the proposed model geometry

Out of these eleven variables, only six are taken as the *independent* parameters. The five variables that are eliminated are:

- Body Radius, R. Since we are interested in the vehicle forebody design, we will unify the forebody base diameter for all designs. The forebody will have a unit diameter.
- Length of the cylindrical part, B. Similarly, this part is not included in the optimization process. It is added to enable investigating the impact of the forebody on the flowfield features downstream of the body shoulder. Thus, it will be given a fixed length of 0.25 of the forebody diameter.
- The spike radius, r_s. It was proved [36-39] that the spike rod radius has a very small effect on its performance within a practical range. Thus, the spike radius will have a fixed value of 0.02 of the forebody diameter.
- Cone semi-apex angles for the forebody and the aerodisk, δ and δ_d, respectively. They are not actually independent variables since they can be expressed in terms of other variables, L, r, L_d, and r_n, respectively, to ensure a tangency of spherical and conical parts.

As a result, only six variables will be taken as the *independent* design parameters. The vector of design parameters is

$$\mathbf{X} = [L \quad r \quad L_S \quad r_d \quad L_d \quad r_n]^T$$

The range of the allowable values of theses design parameters is specified. It is desired to widen this range so as to enrich the variety of shapes. However, very wide ranges result in a large design space, imply large number of samples, and may yield non-realistic geometries. In this work, the following values of the design parameters are adopted (for a unit diameter of the forebody):

$$L = 0.0:1.0 \qquad r = 0.02:0.5 \qquad L_S = 0.1:4.0 \qquad r_d = 0.02:0.1 \qquad L_d = 0:0.15 \qquad r_n = 0.0:0.1$$

To eliminate the effect of different dimensions of the design parameters, they are scaled linearly to the same range namely, $[0,1]$. In what follows, the scaled design parameters are given the same symbols with a prime. Eventually, the design space of the current problem can be viewed as a 6-dimensional unit hypercube with the scaled design parameters on its coordinates. It can be shown that, by independently changing the values of these design parameters, a variety of shapes can be attained. Samples of the possible shapes are illustrated in the figure below.

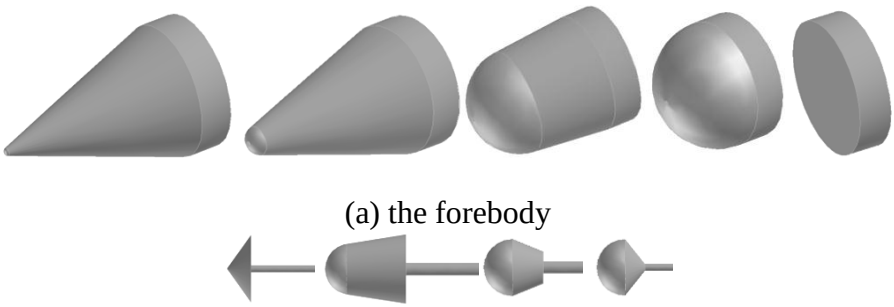

(a) the forebody

(b) the aerodisk

Figure 4 Possible geometries for both the forebody and the aerodisk

B. Sampling Technique, DoE

The next step is to pick the samples from the design space. Here, 200 samples are selected whose high-fidelity responses are calculated by the CFD model and used to construct its surrogate. The sampling technique implemented in this work is the space-filling Latin hypercube sampling (LHS). The standard LHS [40] does not guarantee a perfect space-filling as shown in Fig. 5a, hence, we adopt the Morris-Mitchell (M-M) technique [41] to improve the standard LHS. The MM-enhanced LHS is shown in Fig. 5.b.

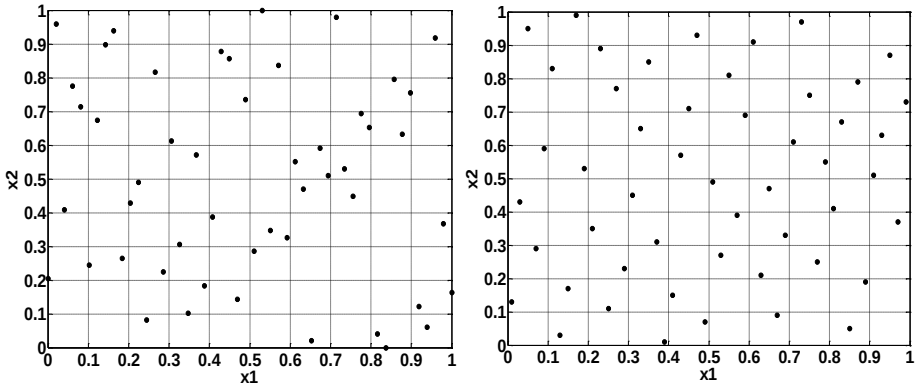

(a) standard LHS (b) MM-LHS

Figure 5 Sample sites in a two-dimensional space using the standard LHS

The SURROGATES toolbox [42] is utilized in this work to select the samples. Here, a genetic algorithm is implemented to optimize the distance between samples according to Morris-Mitchell criteria.

C. Statement of the Optimization Problem

It is desired to optimize the forebody design of a spiked blunt vehicle in hypersonic speeds. The optimization problem in concern involves two design objectives namely, minimizing the drag and minimizing the aerodynamic heating on the forebody. The flow stability is taken as a constraint for the optimization. The optimization is assumed for zero incidence, Mach 6 flight at an altitude of 60 Km in a standard atmosphere [43]. Consequently, the freestream flow conditions are $T_\infty = 247.021K$, $P_\infty = 21.95Pa$, $\rho_\infty = 3.0968\times10^{-4}\ kg/m^3$, $\mu_\infty = 1.5844\times10^{-5}\ kg/m.s$. Based on the forebody diameter and the freestream conditions, the Reynolds number $\mathrm{Re}_{\infty D} = 3.69\times10^4$; the flow is therefore assumed laminar in the whole computational domain.

D. The High-Fidelity CFD Model

Each sample in the design space is in fact a unique design. The performance of all sample designs is evaluated by solving the computational flowfield using the high-fidelity CFD model. The density-based laminar model in Fluent [44] is used in this work. Due to symmetry of both geometries and freestream flow, the computational domain of all cases is an axisymmetric one. The boundaries of the computational domain are illustrated in Fig. 6a for a sample design.

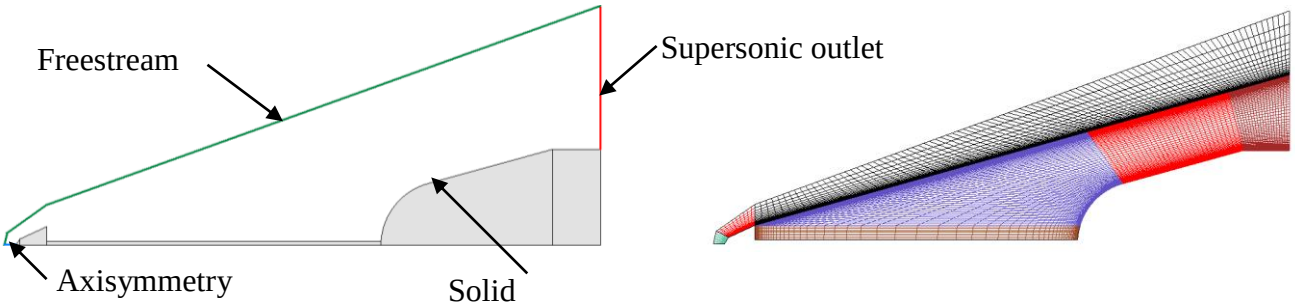

Figure 6 Boundaries and discretization of the computational domain

At the freestream boundary, the flow absolute pressure, static temperature, Mach number, and velocity direction are specified. To minimize the computational cost, the undisturbed freestream conditions are specified as close as possible to the foreshock wave generated at the spike tip. The upstream and lateral extents of the freestream boundary vary from one sample to the other depending on its design. A supersonic outlet boundary is allocated at the flow exit where its total temperature and static pressure are specified whereas an axisymmetric boundary is allocated at the centre line of the design. At the solid walls, no-slip condition is applied. The walls are assumed isothermal with a temperature equals to the freestream one. To generate the discretised computational domain, a multi-block structured grid is constructed. The grid is intended to be clustered along the expected position of the foreshock wave generated at the spike tip as well as near the walls. This feature-aligned grid yields a better solution of the shock wave and hence, the overall numerical simulation is expected to be more accurate. Hence, the location of clustered grid varies from one sample to the other depending on its design. The geometry is designed and the grid is constructed using Gambit [45]. A sample grid is illustrated in Fig. 6b; the density of the grid is reduced for better illustration.

To validate the numerical solver, three different experimental cases are selected. The first case is selected from the experimental investigations by Crawford [21]. In the experiment, both surface pressure and heat transfer to a hemisphere-cylindrical model of $(L/D=2)$ were measured. The freestream Mach and Reynolds numbers were $M_\infty = 6.8$ and $\mathrm{Re}_{\infty D} = 0.13\times10^6$, respectively. The pressure drag coefficient was calculated by integrating the absolute pressure along the model. To test the grid sensitivity, four grids with different resolutions were examined. The pressure drag coefficients calculated using these grids are listed in Table 1. The minimum cell height refers to the cells at the solid wall and in the clustered shock-aligned zones. The value of the pressure drag converges with a satisfactory accuracy. The very-fine grid setup yields a pressure drag value very close to the experimental one. It is thus used for all samples.

Table 1 Variation of pressure drag coefficient with mesh resolution

Source	Coarse	medium	fine	very-fine	Experiment, [21]
Min. cell height	$10^{-3}D$	$10^{-3}D$	$8\times10^{-4}D$	$10^{-4}D$	
Total no. of cells	45000	80000	250000	350000	
Pressure drag coefficient	0.323	0.291	0.219	0.211	0.21

In addition, the profiles of pressure and heat flux variation along the hemispherical part of the body using the very-fine grid are plotted in Fig. 7a and 7b, respectively. The experimental pressure profile is accurately predicted by the flow solver. In addition, the location and the value of the peak heat flux are captured well. The trend of heat flux profile is captured well ahead of reattachment. However, the large discrepancies between the measured and calculated heat flux values downstream of reattachment may be an indication of boundary layer transition in the experiment which was addressed by Crawford [21].The general flow features namely, the foreshock, the shear layer, and the reattachment shock are capture accurately as inferred from the computed radial density gradient contours compared with Schlieren photograph of the experiment in Fig. 7c.

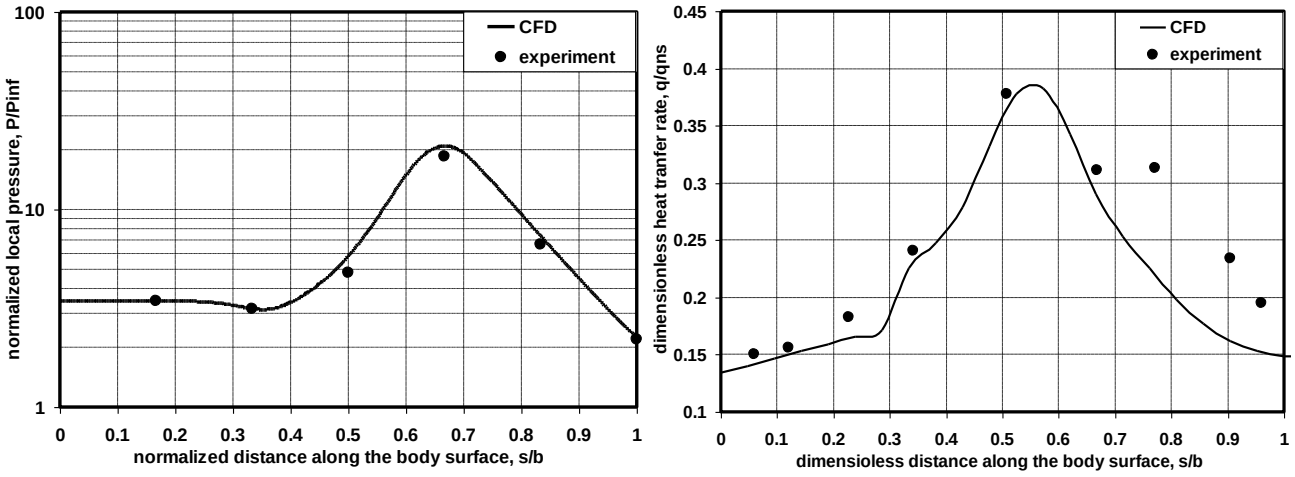

(a) (b)

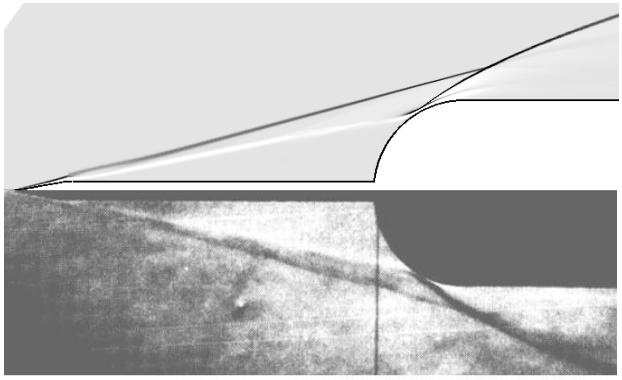

(c)

Figure 7 Validation results of test case 1

Another model from the experiments by Gnemmi et al. [4] is selected. The model is a hemisphere cylinder equipped with a spike and a biconical aerodisk with $L/D=1$. The

freestream Mach and Reynolds numbers are $M_\infty = 4.5$ and $\mathrm{Re}_{\infty D} = 4.8\times10^6$, respectively. The study focused on visualizing the flowfield and the drag variation at different incidences. The $RNG-k-\varepsilon$ turbulence model is implemented in the numerical simulation and radial density gradient contours as evaluated by the flow solver are compared with the experimental Schlieren photograph in Fig. 3. Clearly, the flow solver manages to capture the flowfield features. The locations of shear layer reattachment and foreshock- reattachment shock intersection are accurately calculated. The last validation test case is selected from the experimental work by Kalimuthu et al. [17]. The model is a hemisphere cylinder equipped with a spike of $L/D = 1.5$ and a hemispherical aerodisk of $d/D = 0.2$. The freestream conditions of the experiment correspond to Mach 6 and Reynolds number of 0.15×10^6. The study focused on the variation of the flowfield features and the aerodynamic coefficients with incidence. The axial density gradient contours as calculated by the laminar flow solver are compared with the Schlieren picture in Fig. 4. The features of the flowfield are accurately captured by the flow solver.

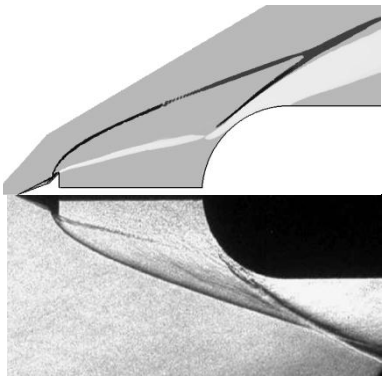

Figure 3 Validation results of test case 2

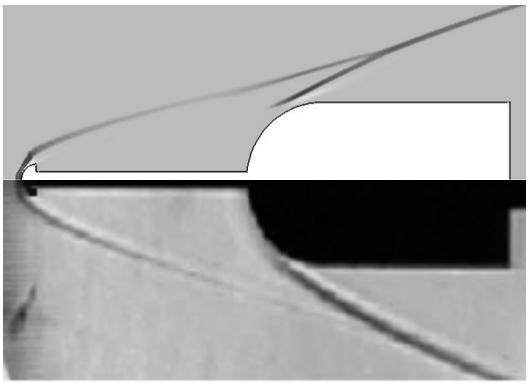

Figure 4 Validation results of test case 3

E. Metrics of Performance

Three values of the CFD output are taken as the performance metrics associated with the prescribed objectives and constraint. The total drag coefficient (referred to the freestream conditions and the base area of the forebody) is taken as the measure for the drag objective. The peak heat transfer rate to the forebody is taken as a metric for the aeroheating objective. In a previous small-scale optimization study by the authors [35] involving two design parameters only, the stability constraint was satisfied by simply limiting the range of variation of the spike length. However, in the present full-scale problem, relating the instability to the design parameters is not as straightforward. Hence, the stability is introduced as an explicit constraint function. Initially, the flow around all samples is calculated using a steady solver. Samples that yield a variation in the drag coefficient below 1 drag count are considered stable. The flow solution of other samples is then switched to the unsteady solver to eliminate the uncertainty about whether the source of flow unsteadiness is due to numerical errors or real (physical) instability. The amplitude of variation in the drag coefficient with iterations after convergence (or simulation time) is taken as the metric for the stability constraint. For these samples, the mean values of the drag coefficient and the peak heat flux are taken as the metrics for drag and aeroheating objectives, respectively.

F. The surrogate model

For each of the objective and constraint functions, a separate surrogate is constructed using Kriging. Kriging is one of the most powerful and flexible surrogates which was originally introduced by D. G. Krige in the field of geology [46]. It was later developed by Matheron

[47] and made popular in computer-based experiments by Sacks et al. [48,49]. In Kriging, the response of the surrogate, $\hat{y}(\mathbf{x})$, at a given design point, $\mathbf{x}$, can have a variety of forms. However, ordinary Kriging is the most popular Kriging surrogate in ADO applications [50,51]. In this model, the response is expressed as the sum of constant mean and localized deviations at the training samples:

$$\hat{y}(\mathbf{x}) = \beta + z(\mathbf{x}) \approx y \tag{1}$$

where y represents the high-fidelity response and $z(\mathbf{x})$ is the realization of a random process with zero mean, variance σ^2, and covariance:

$$Cov(z) = \sigma^2 \mathbf{R}(\mathbf{x}^i, \mathbf{x}^j) \tag{2}$$

The correlation matrix $\mathbf{R}(\mathbf{x}^i, \mathbf{x}^j)$ is an $n \times n$ symmetric matrix whose elements are expressed in terms of the spatial correlation function of any two samples, $\mathbf{x}^i$ and $\mathbf{x}^j$. The exponential form of this correlation:

$$scf(d) = \exp(-\theta \times d^p), \tag{3}$$

where d is the Euclidian distance between the two samples, is widely used in engineering applications since it adds continuity, smoothness and differentiability to the surrogate model [51,52]. It is also more accurate when applied to multimodal or random responses [53]. β, θ, and p are the undetermined parameters of the Kriging surrogate that are evaluated by maximizing the likelihood estimation (MLE). The MLE for the mean trend parameter, β is:

$$\hat{\beta} = \left[\mathbf{A}^T \mathbf{R}^{-1} \mathbf{A}\right]^{-1} \mathbf{A}^T \mathbf{R}^{-1} \mathbf{y} \tag{4}$$

where $\mathbf{A}$ and $\mathbf{y}$ are the Vandermonde matrix and the vector of the high-fidelity responses of the training samples. On the other hand, the MLE values of θ and p are evaluated using the formula:

$$-\frac{1}{2}\left[n \ln \hat{\sigma}^2 + \ln|\mathbf{R}|\right] \tag{5}$$

where $\hat{\sigma}^2$ is the MLE value of the variance expressed as:

$$\hat{\sigma}^2 = \frac{1}{n}(\mathbf{y} - \mathbf{A}\boldsymbol{\beta})^T \mathbf{R}^{-1}(\mathbf{y} - \mathbf{A}\boldsymbol{\beta}) \tag{6}$$

where n is the number of training samples. The response of the Kriging surrogate at a new sample $\bar{\mathbf{x}}$ is evaluated by as:

$$\hat{y}(\bar{\mathbf{x}}) = \beta + \mathbf{r}^T(\bar{\mathbf{x}})\mathbf{R}^{-1}(\mathbf{y} - \mathbf{A}\boldsymbol{\beta}), \tag{7}$$

where $\mathbf{r}$ is the correlation vector between the new point and all training samples. In this work, the SURROGATE toolbox [42] is used to construct the Kriging model. The tuning of the undetermined parameters, θ and p is done iteratively similar to the approach proposed by Jeong et al. [54]. In this approach, initial values are assigned for the parameters and the equations (4) and (6) are solved iteratively until convergence is attained. To validate this toolbox, the two-dimensional Rastrigin test function is used. The exact expression of this function is [55]:

$$z(x,y) = x^2 + y^2 - 0.5\left[\cos(2\pi x) + \cos(2\pi y)\right] + 1, \qquad x, y \in [-2.5, 2.5] \tag{8}$$

Figure 8 below illustrates the three-dimensional and contour plots of both the exact and the Kriging surrogate using 100 samples. The high quality of Kriging surrogate and the accuracy of the toolbox are clearly evident.

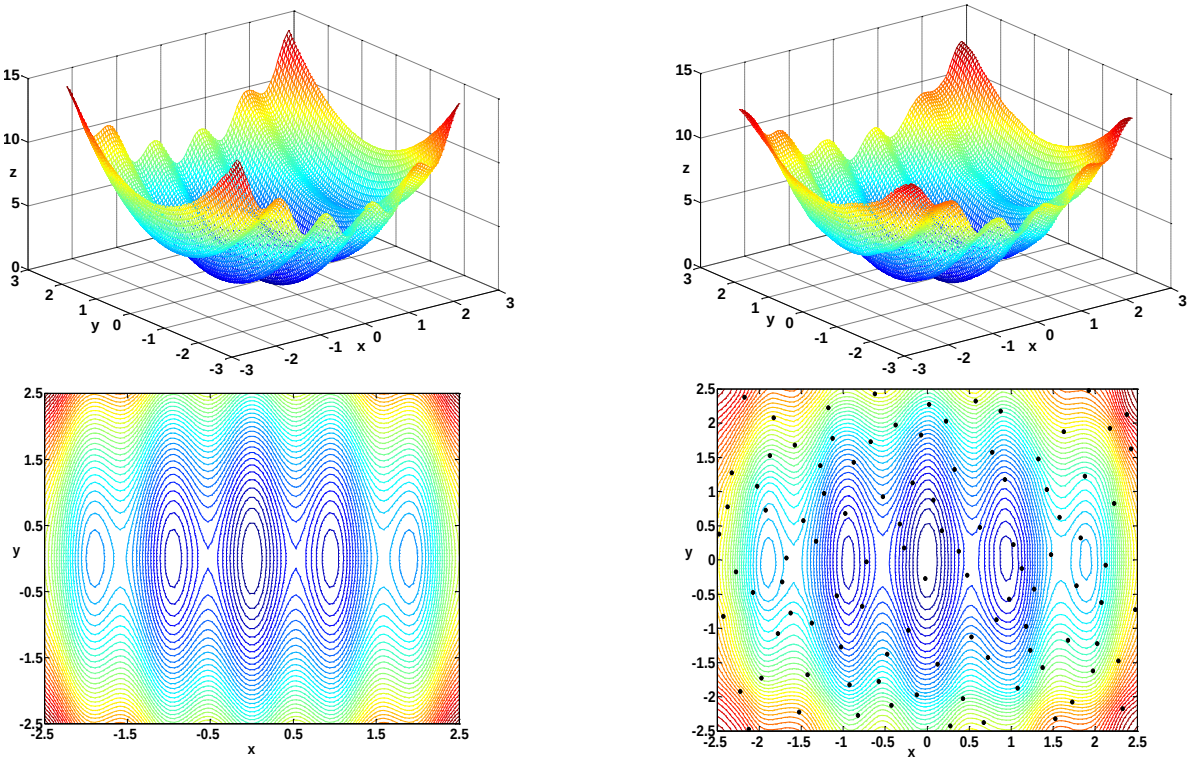

(a) the exact function (b) Kriging surrogate

Figure 8 Kriging prediction of Rastrigin test function

G. The Multi-objective Evolutionary Algorithm

The elitist non-dominated sorting genetic algorithm, NSGA-II [56], was developed as an improvement for its predecessor, NSGA, by adding the elitist preservation. It is a multi-objective technique based on the genetic algorithm, GA, in which the optimality of an individual is defined by its dominance (rank) with respect to other individuals in the population. NSGA-II starts by generating a randomly selected population, P, of size N from the design space and their associated fitness vector is evaluated. When coupled with a surrogate, the response of the latter is used as the fitness value. Next, the algorithm acts in the following steps:

Step1: Non-domination sorting. All individuals are sorted according to their dominance levels. The individuals that are non-dominated by any other individual in the population are given the lowest rank; $r = 1$. These are the members of the first Pareto front. The remaining individuals are considered and the set of non-dominated solutions are given a higher rank; $r = 2$. These are the individuals of the second Pareto front. The process is applied to the whole population. Eventually, the population is divided into layers of Pareto fronts. Individuals in each front are assigned the same rank.

Step2: Binary tournament selection. Individuals are then selected for GA operations by comparing all individuals in pairs. The selection takes the dominance, feasibility, and crowdedness of the individuals into consideration as follows. For a pair of solutions, the feasible one wins the tournament. If both solutions are infeasible, the one that is less violating wins the tournament. The individual's violation is calculated as the sum of violation of all

constraints. If both solutions are feasible, the one with a lower rank wins. If both solutions are feasible and have the same rank (belong to the same Pareto front), the one that has a larger crowding distance wins the tournament. The crowding distance of an individual, $\mathbf{x}$, is the length of the semi-perimeter of the l-dimensional hypercuboid enclosing $\mathbf{x}$ with its vertices located at the nearest neighbouring individuals in the objective space, where l is the number of objectives.

Step3: GA operations. The crossover and mutation operators are applied to the selected N individual to generate the offspring.

Step4: Elite preservation. The parents are allowed to compete with their offspring by merging both generations in one population of size $2N$. Go to step1 and the process cycles until convergence is attained.

The NSGA-II toolbox [57] is used in this work. To validate this tool, a test problem involving two objective functions is used. The ZDT3 problem [55] is characterized by a discontinuous convex Pareto surface and is expressed as follows:

$$f_1(\mathbf{x}) = x_1 \text{ , and } \qquad f_2(\mathbf{x}) = g(\mathbf{x})h(\mathbf{x}) \tag{9}$$

where $g(\mathbf{x}) = 1 + \frac{9}{n-1}\sum_{i=2}^{n} x_i$ and $h(\mathbf{x}) = 1 - \sqrt{f_1/g} - (f_1/g)\sin(10\pi f_1)$

such that $x_i \in [0,1]$ and $n = 30$. Figure 9 illustrates the real Pareto surface and that predicted by NSGA-II toolbox. Here, 100 individuals were used and the solution converged after 3000 generations. The features of a good Pareto representation namely, convergence, wide spread, and uniformity [58,59] are achieved.

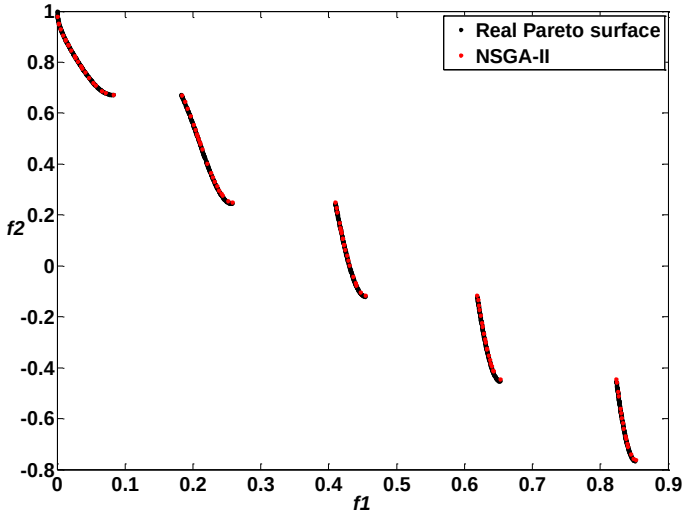

Figure 9 Test function for NSGA-II toolbox

H. Framework of the Study

The design space is constructed in Matlab [60] platform based on the predefined ranges of design parameters and the number of samples. To ensure a good-quality grid for all samples with diverse designs, the grids are constructed manually. Then all CFD cases are run in parallel. The convergence of all CFD cases is supervised individually to ensure reliable high-fidelity response values. The Fluent journal files are designed to write the desired output values in separate text files. A Fortran code collects the responses of all samples in separate files that are then transferred to Matlab for metamodelling and optimization steps.

III. Results and discussions

A. Objective Space of the Training Samples

The locations of the 200 training samples in the objective space are illustrated in Fig. 10. The samples show a degree of competition between the two design objectives. The blue and red dots refer to models that yield stable and unstable flow, respectively.

In the small-scale optimization, the flow instability was also associated with high drag and aeroheating values. However, in this full-scale optimization, the flow instability seems to be not associated with a specific performance of the samples. The design can have a stable or unstable flow with low or high values of the performance metrics. Nonetheless, unstable models are commonly characterized by medium or high aeroheating levels. A focus is made on a number of samples that show extreme performance. They are marked and numbered in Fig. 10.

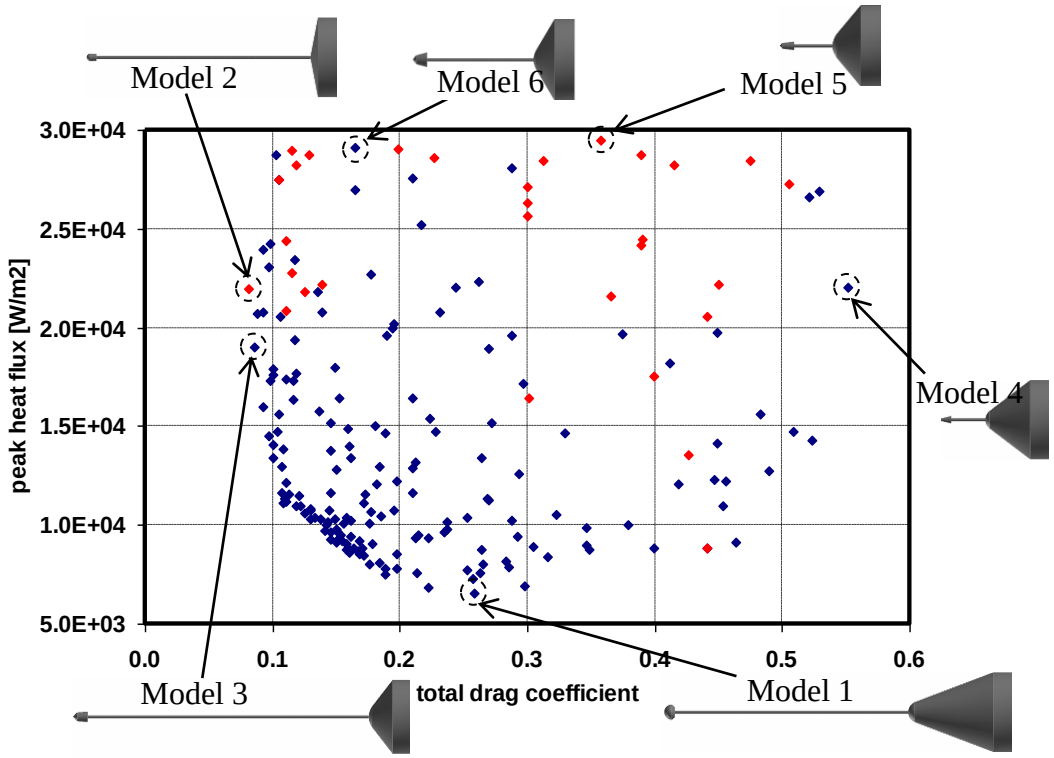

Figure 10 Locations of the training samples in the objective space

Model 1 yields the least peak heat flux among all training samples. It is also characterised by a stable flow and a relatively low drag. The flowfield features of this model are illustrated in Fig. 11a where the upper and lower halves show the calculated velocity and pressure contours, respectively.

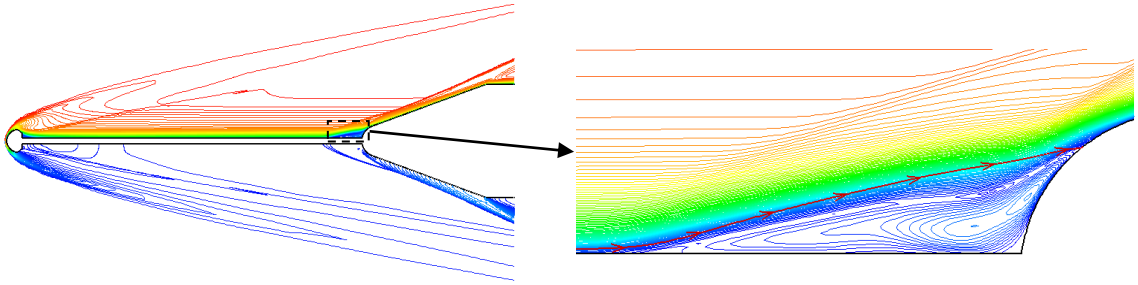

(a) (b)

Figure 11 Features of the computed flowfield around model 1

The shear layer separates at the aerodisk shoulder and reattaches on the relatively long spike engulfing a very small recirculation zone at the aerodisk base. Since the forebody is slender ($L' = 0.9598$) and its nose radius is relatively small, the shear layer remains attached to the spike until it separates immediately upstream on the forebody forming a small recirculation zone. Details of the velocity contours at this region are illustrated in the close-up in Fig. 11b. The red arrowed line indicates the dividing streamline that links the separation and reattachment points of the shear layer [61]. According to Holden [27], the aeroheating at reattachment is mainly governed by the "reattachment flow geometry". In model 1, the shear layer is almost parallel to the forebody surface at reattachment. Hence, the "smooth", low-strength, reattachment of the shear layer on the forebody nose and the low velocity gradients of the reattaching boundary layer contribute in the low value of peak heat flux. However, as the low-pressure flow downstream of the spike's aerodisk approaches the forebody, two successive oblique shock waves are created due to the shear layer separation and its reattachment. The high pressure values attained by the flow downstream of these two shock waves along with a small area of the forebody being screened by the small low-pressure recirculation zone are responsible for the rise in the drag coefficient on this model.

Model 2 produces the least drag coefficient among the training samples. It is also characterised by a high aeroheating value. However, the flow around it is unsteady. The instantaneous features of the flowfield around this model are illustrated in Fig. 12a where the computed velocity and pressure contours are plotted in the upper and lower halves, respectively.

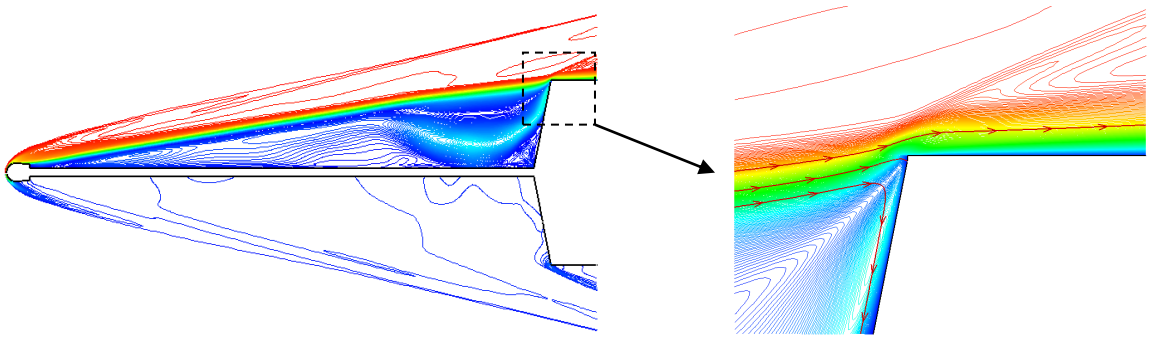

(a) (b)

Figure 12 Features of the numerical flowfield around model 2

The relatively blunt aerodisk tip and large aerodisk base radius encourage the separation of the shear layer at the aerodisk shoulder. The medium spike length ($L_S' = 0.6784$) and the highly blunt forebody face encourage the shear layer to propagate directly to the forebody shoulder without reattaching on the spike. At the forebody shoulder, the shear layer performs a partial reattachment. A partial reattachment means that part of the streamlines constituting the shear layer reverse into the recirculation zone, others escape past the forebody shoulder, whereas the dividing stream line always stagnates at the forebody shoulder as illustrated by Wood [62]. A close-up on the flow details in this area are illustrated in Fig. 12b. The resulting large recirculation zone screens the entire area of the forebody face causing the surface pressure and, consequently, the drag to become significantly low. However, as indicated by Wood [62], this arrangement of shear layer reattachment invokes flow instability in the form of lateral oscillations of the shear layer. On the other hand, the strong reattachment of the shear layer on the nearly-flat forebody face causes the peak aeroheating flux to attain a relatively high value.

Model 3 produces a near-minimum drag, relatively high aeroheating, and more importantly, a stable flowfield. The computed velocity and pressure contours of model 3 are illustrated in the upper and lower halves of Fig. 13.

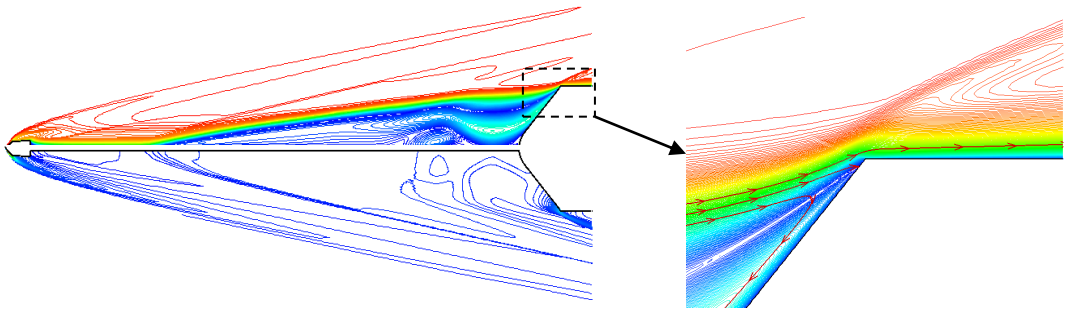

(a) (b)

Figure 13 Features of the numerical flowfield around model 3

Similar to model 2, the shear layer in model 3 partially reattaches on the forebody shoulder with the dividing streamline always reattaching on the forebody. The main difference between models 2 and 4 is that the latter has a less inclined forebody face. This enhances a stable reattachment of the shear layer. As stated by Holden [27], the shoulder reattachment can be stable or unstable depending on the face inclination and the spike length. Model 3 has a longer spike and a less inclined forebody face; both features stabilize the reattachment which is consistent with [9]. The slightly higher drag in model 3 may be due to the higher friction on the longer aerodisk and spike. The peak heat flux of model 3 is also less than that of model 2. This may be explained by its smaller inclination which makes the reattachment of the shear layer slightly smoother.

Comparing models 1, 2, and 3, we can deduce that a long spike is preferred for both low drag and aeroheating. In addition, the flow stability depends on the shape of both the spike and forebody face. While the location of shear layer reattachment dictates the drag value, the strength of this reattachment dictates the aeroheating value. Finally, we can infer that, a blunt forebody yields less drag, a slender one produces more drag, and the opposite is true for aeroheating. This feature of spiked bodies is in an interesting contrast to the unspiked ones.

Model 4 yields the highest values of drag among the training samples. It is also characterised by high aeroheating levels and stable flowfields. The flowfield features of this model are illustrated in Fig. 14.

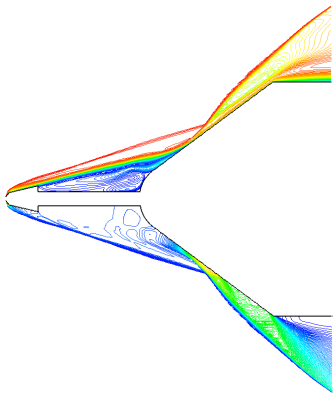

Figure 14 Features of the numerical flowfield around model 4

The shear layer separates at the aerodisk shoulder encouraged by the vicinity of the forebody (due to very short spikes). The shear layer reattaches on the forebody face away from its shoulder. This face reattachment yields a stable flowfield as illustrated by Holden [27]. The exposed part of the forebody generates a strong bow shock that intersects with both the shear

layer and foreshock. Since the spike is short, this intersection takes place ahead of the forebody face producing high levels of flow pressure and yielding high drag.
Model 5 yields the highest peak heat flux among all training samples. It is characterized by a relatively high drag and unstable flowfield whose instantaneous features are illustrated in Fig. 15a.

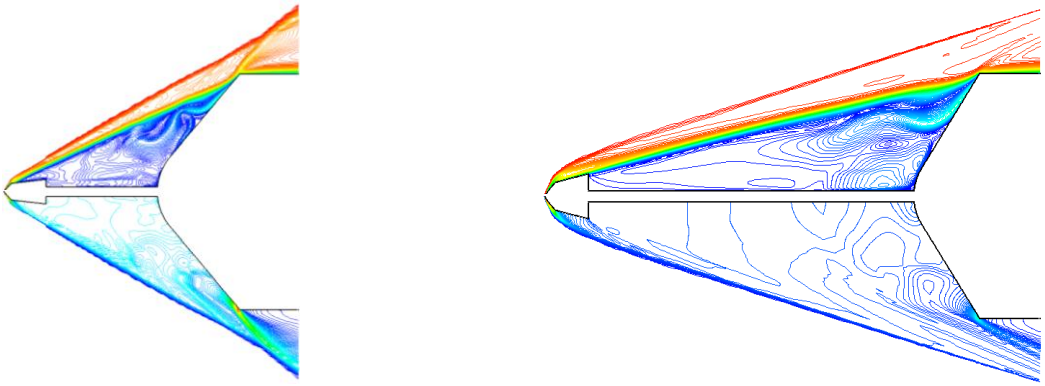

(a) (b)

Figure 15 Features of the numerical flowfield around models 5 and 6

The forebody face of model 5 is more inclined compared with model 4. The shear layer separates at downstream of the aerodisk tip and reattaches partially at the forebody shoulder. The short spike and the inclined face result in a strong reattachment which explains the elevated level of aeroheating. The flow instability may be explained by the interaction between the reattaching shock wave and the strong reattachment shock. The high drag is explained by the high inclination of the foreshock and the effective body outlined by the shear layer. Further increasing the spike length produces a weaker foreshock and a more slender effective body which reduces the drag as in the case of model 6. Model 6 also yields the highest aeroheating among samples that maintain a stable flow. Its flowfield features are illustrated in Fig. 15b. In addition to longer spike, the larger aerodisk further increase the slenderness of the effective body and reduces the strength of the reattachment shock despite that the forebody face is more inclined compared with model 5. The reattachment geometry of this model explains the high peak heating value.
Comparing the features of the models above, we can deduce that a long spike is preferred for both low drag and aeroheating. In addition, while the inclination of the shear layer and its reattachment location dictate the drag value, the strength of this reattachment dictates the aeroheating value. The strength of reattachment generally corresponds to its "geometry" based on the inclination of both the shear layer and the forebody face. In addition, the flow instability depends on the shape of both the spike and forebody face and is generally associated with highly-inclined forebody faces. Finally, we can infer that, if a long spike is used, a blunt forebody yields less drag, a slender one produces more drag, and the opposite is true for aeroheating. This feature of spiked bodies is in an interesting contrast with the unspiked ones.

B. Surrogate Assessment and Enhancement

Next, based on the CFD values of the performance metrics for the training samples, three surrogates are constructed representing the total drag coefficient, peak heat flux, and the amplitude of variation of the total drag coefficient. The accuracy of the surrogates is assessed using the cross validation technique. In this technique, no new test samples are required and small subsets of the training samples are used to assess the accuracy of the surrogate which is constructed using the remaining training samples. In this work, each assessment subset

includes one sample which means that the accuracy is calculated at all samples. The surrogates constructed on the training samples showed a relatively unsatisfactory accuracy. To improve the accuracy of the surrogates, new samples are added at the minimum point of the surrogate as follows. Each of the drag and aeroheating surrogates is individually coupled with the single-objective GA available in Matlab. The located optimum design in each is evaluated by the CFD solver, the new design and its high-fidelity response are added to the training samples for both surrogates, and the two surrogates are reconstructed. This process is done iteratively and a satisfactory accuracy is attained after 32 iterations. Since this is done for both drag and aeroheating responses, each of the three surrogates is effectively augmented by 64 new data points. Such approach yielded a significant improvement in the surrogate's accuracy. For instance, the evolution of aeroheating surrogate accuracy with the added samples is illustrated in Fig. 16.

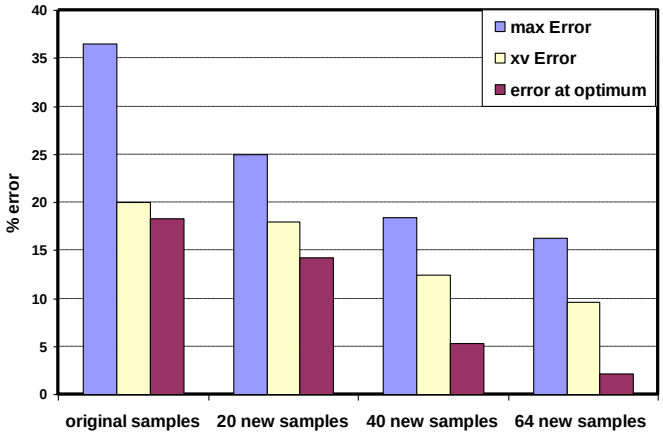

Figure 16 Evolution of aeroheating surrogate accuracy

The maximum absolute and the cross-validation (xv) errors are compared with the mean value of aeroheating of all training samples whereas the error at the optimum location is compared with the CFD value.

C. Sensitivity Analysis

The role of each design parameter in determining the model performance can be roughly inferred from the corresponding values of the parameter θ [63]. They are listed in Table 2.

Table 2 Values of θ for the design parameters

	L'	r'	L'_s	r'_d	L'_d	r'_n
Drag	0.502654	0.745874	1.115698	0.29547	0.14	0.445178
Aeroheating	0.57	0.341587	0.18522	0.09965	0.072354	0.22
Flow stability	2.322	0.81125	3.66	0.31842	0.15026	0.55264

A larger value of θ indicates a higher importance of the design parameter. Nevertheless, the dependence of a design performance on its design parameters can be more accurately computed via Sobol's total sensitivity indices [64]. Figure 17 illustrates these indices for each design parameter in both design objectives and constraint using the SURROGATE toolbox.
The drag objective is mainly dominated by the spike length. The spike length also has a major role in determining both the aeroheating and flow stability. The role of the forebody nose radius is more pronounced in aeroheating than in drag and stability. The design of the aerodisk shows a minor influence on the objectives and constraint values. The aerodisk nose radius is the most important parameter of the aerodisk while its length is the least important.

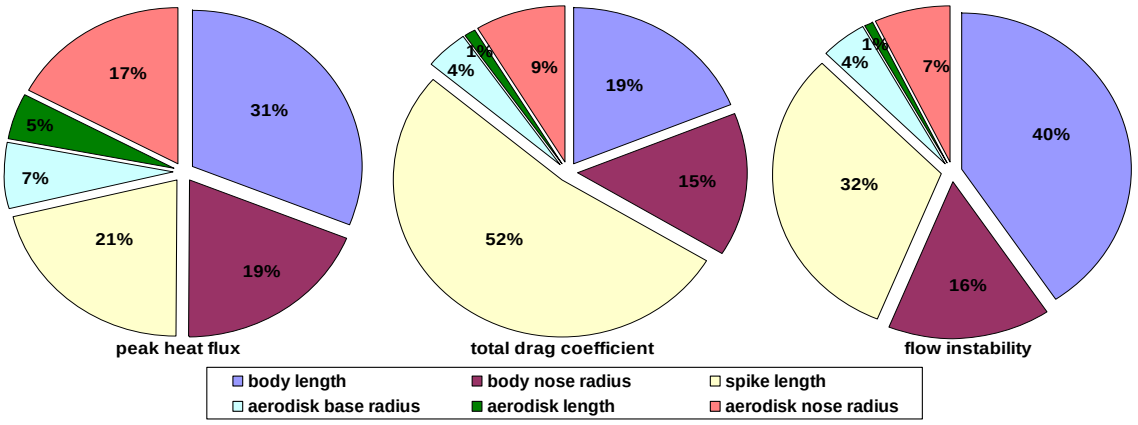

Figure 17 Sobol's total sensitivity indices of the design parameters in the optimization objectives and constraint

B. Optimization Results: the Pareto Optimal Designs

Finally, the multiobjective optimization is conducted. Two optimization problems are considered namely, unconstrained and constrained optimization problems. The impact of population size and generations number is tested and the solution is found to converge to the Pareto surface after 1000 generations using 1000 individuals. The locations of the Pareto optimal solutions in the objective space, the Pareto fronts, for both optimization problems are illustrated in Fig. 18.

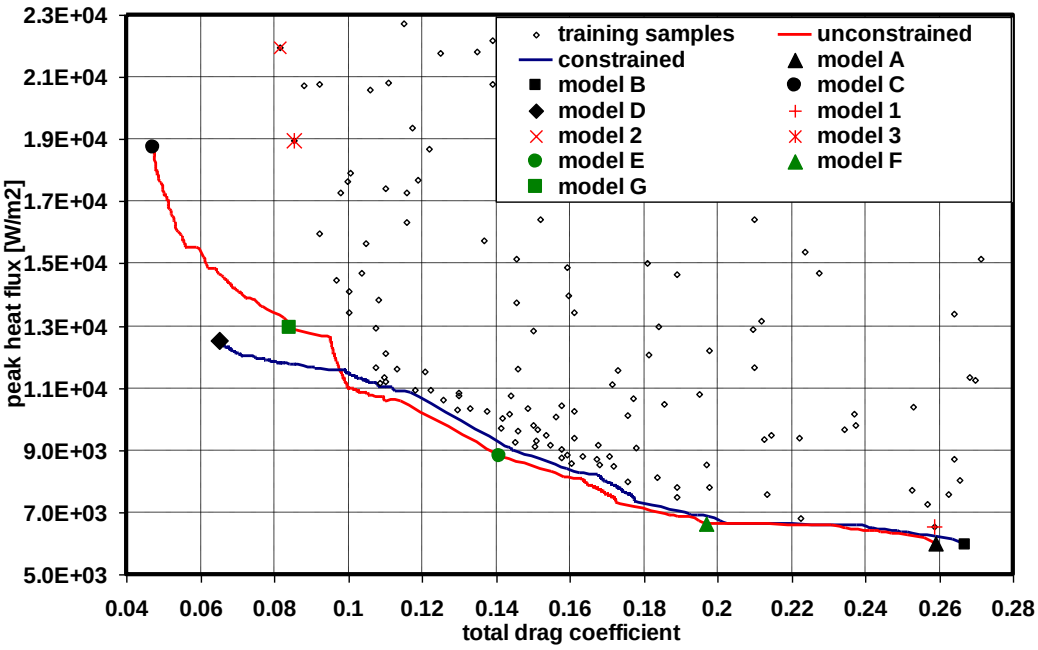

Figure 18 Pareto front of the optimization problem

Compared with the original training samples, the Pareto optimal designs of both problems show a considerable performance improvement in both objectives. Here, the focus is on a number of key samples.

Models A and B lie on the aeroheating minimum of unconstrained and constrained Pareto fronts, respectively. The flow features of these models are illustrated in Fig. 19.

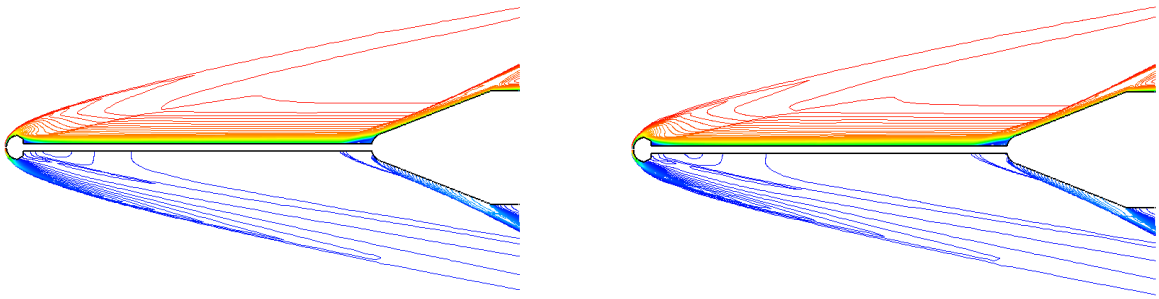

(a) (b)

Figure 19 Features of the numerical flowfield around (a) model A, and (b) model B

The flow in both models shows almost the same features. The blunt aerodisk generates a detached bow shock ahead of it. The boundary layer separates at the aerodisk shoulder, reattaches on the spike, and remains attached. Immediately ahead of the forebody the shear layer separates and reattaches on the forebody forming a small recirculation zone. Two small shock waves are created at shear layer terminal separation and reattachment ahead of the forebody. In fact, models A and B seem identical to each other and to Model 1 of the training samples. The dimensionless design parameters and performance metrics as calculated by both the surrogate (KG) and the CFD model are compared with those of model 1 in Table 3.

Table 3 A comparison between the optimum samples and the best training sample for aeroheating

Model	Design parameters						Peak heat flux, W/m^2		Drag coefficient	
	L'	r'	L'_s	r'_d	L'_d	r'_n	KG	CFD	KG	CFD
1	0.959	0.241	0.744	0.578	0.251	0.965		6546.3		0.2586
A	0.935	0.206	0.774	0.563	0.401	0.965	5971.9	6251.2	0.2589	0.2739
B	0.955	0.206	0.774	0.563	0.357	0.965	6015.3	6383.7	0.267	0.264

As inferred from the sensitivity study, the aeroheating depends mainly on the forebody geometry. The forebody of models A and B are shorter and their noses are less blunt compared with model 1. This leads to a smoother reattachment of the shear layer on the forebody nose. Hence, the peak heat flux is reduced. The aeroheating values in models A and B are very close; the CFD value in model B is 2% higher. This may be explained by two factors. First, the slightly shorter aerodisk length creates a wider expansion fan at the aerodisk base (for the same aerodisk nose and base radii). This wider expansion slightly increases the downstream. Second, model B has a slightly more slender forebody (due to the slightly longer forebody) which slightly reduces the flow deceleration ahead of it. Both minor factors may cause the negligible rise in aeroheating on model B. Comparing the high-fidelity values, the reduction in aeroheating is 4.5% compared with the best training samples. The heat flux surrogate shows a high accuracy in predicting the optimum value of aeroheating. Compared with the CFD value, the surrogate underestimates the aeroheating by about 4.4% and 5.8% in models A and B, respectively. On the other hand, both models A and B produce a higher drag compared with model 1. This may be explained by three factors. First, both models A and B have a slightly longer spike which adds to the friction drag on the spike surface. Second, the forebodies of models A and B are shorter with smaller nose radii. This slightly delays the shear layer separation and yields a slightly smaller recirculation zone. Thus, a smaller part of the forebody will be exposed to the low-pressure flow in this zone. Finally, the forebodies of

models A and B are less slender due to shorter bodies and smaller nose radii. This makes the separation and reattachment shocks slightly stronger. This may also explain the slightly higher drag in model A compared with model B. The overall outcome of these three factors is a slight increase in total drag. Compared with the CFD value, the drag surrogate underestimated the drag value of model A and B by less than 4%.

Model C lies on the lower drag extreme of the unconstrained Pareto front. The computed velocity and pressure contours of this model are plotted in the upper and lower halves of Fig. 20, respectively.

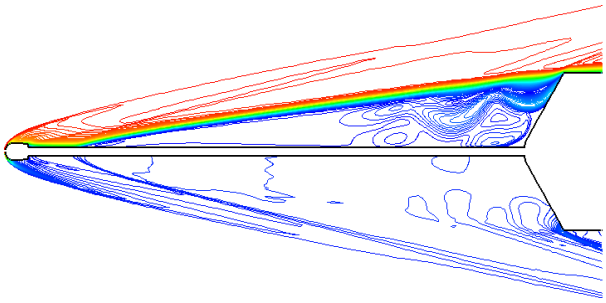

Figure 20 Features of the numerical flowfield around model C

A bow shock wave is generated ahead of the blunt aerodisk. The boundary layer separates early from the spike under the influence of the highly inclined forebody face. The shear layer reattaches at the forebody shoulder. Two shock waves are created at the point of separation and reattachment of the shear layer. Again, model C is similar to model 2 of the training samples. Table 4 illustrates the differences between the two models.

Table 4 A comparison between the unconstrained optimum sample and the best training sample for drag

Model	Design parameters						Drag coefficient		Peak heat flux, W/m^2	
	L'	r'	L'_s	r'_d	L'_d	r'_n	KG	CFD	KG	CFD
C	0.091	0.305	0.806	0.278	0.656	0.469	0.0473	0.0577	18437	20114
2	0.040	0.075	0.678	0.286	0.537	0.477		0.0814		21954

The slightly lower drag of model C can be explained by three factors. First, the aerodisk in model C is longer and its nose and base radii are smaller. The weaker foreshock at the aerodisk tip and the wider flow expansion over it yield a lower downstream flow pressure and a smaller aerodisk base drag. Second, the forebody of model C is slightly more slender due to its longer conical part and larger nose radius. This reduces the level of the flow pressure ahead of it. Finally, the longer spike of model C encourages the early separation of the shear layer which makes the separation shock waves slightly milder. The overall effect is a slight reduction in total drag coefficient. The peak heat flux of model B is slightly lower than that of model 2. This may be due to the slightly milder reattachment on the less inclined forebody face of model C. The drag surrogate underestimated the minimum drag value with an error of 18% compared with the CFD value whereas the aeroheating surrogate overestimated the heat flux with an error of 8.3%. This relatively high error may be due to the uncertainty of the training samples' and the optimum values. Recall that the time-averaged values of the training samples are used in this "basin" of the design space.

Model D is located on the lower drag extreme of the stability-constrained Pareto front. The numerical flowfield features are illustrated in Fig. 21.

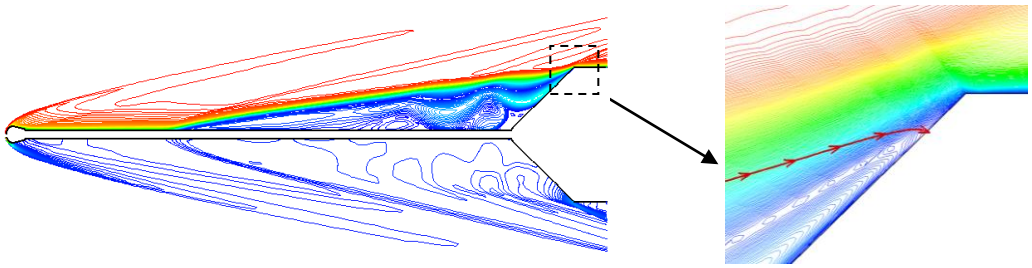

Figure 21 Features of the numerical flowfield around model D

A bow shock is generated at the aerodisk blunt tip. The shear layer separates well ahead of the forebody and reattaches partially at its shoulder. The close-up at the forebody shoulder indicates that the reattachment point is well below the acute corner. The differences between model D and model 3 of the training samples are illustrated in Table 5.

Table 5 A comparison between the constrained optimum sample and the best training sample for drag

Model	Design parameters						Drag coefficient		Peak heat flux, W/m^2	
	L'	r'	L'_s	r'_d	L'_d	r'_n	KG	CFD	KG	CFD
D	0.408	0.108	0.919	0.144	0.568	0.543	0.065	0.074	12536	14552
3	0.100	0.442	0.975	0.638	0.945	0.603		0.0854		18985

The forebody of model D is longer and its nose radius is smaller. Overall, the forebody of model D is slightly more slender than model 3 which explains the lower peak heat flux value. In both models, the low inclination of the forebody face stabilizes the reattachment and yields stable flow features. The lower drag on model D may be due to a number of factors. The aerodisk geometry of model D yields a weaker foreshock and a lower pressure on its base. In addition, the shorter spike of model D produces lower friction drag. Finally, the less-inclined forebody face of model D produces a lower pressure field ahead of it.

Model E is a sample of the intermediate models lying between the Pareto extremes. The computed velocity and pressure contours are illustrated in the upper and lower halves of Fig. 22 whereas its dimensionless design parameters and performance values are listed in Table 6.

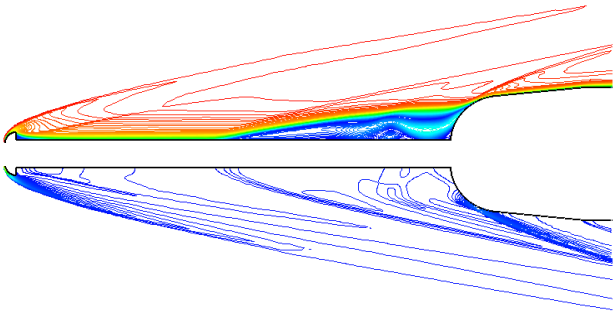

Figure 22 Features of the numerical flowfield around model E

A bow shock is created at the blunt aerodisk and a small recirculation zone is engulfed at its base by the shear layer that separates at the aerodisk shoulder. As the shear layer reattaches on the spike downstream of the aerodisk, a small internal shock wave is created. The bluntness of the forebody encourages the early separation of the shear layer from the spike and the

formation of a relatively large recirculation zone. The long spike decelerates the flow velocity inside the shear layer and the curvature at the reattachment zone yields a smooth reattachment. Both factors contribute to the low peak heat flux value on this model. The relatively low drag on this model can be explained by two factors. On one hand, a considerable portion of the forebody face is screened by the large low-pressure recirculation zone. On the other hand, the low inclination of the forebody generates a weak reattachment shock wave which yields a low flow pressure at and downstream of reattachment.

Table 6 Design parameters and performance values for model E

Model	Design parameters						Drag coefficient		Peak heat flux, W/m^2	
	L'	r'	L'_s	r'_d	L'_d	r'_n	KG	CFD	KG	CFD
E	0.698	0.844	0.924	0.334	0.02	0.888	0.141	0.123	8809	7898.3

As the optimal design evolves from model E towards models A and B, the slenderness of the forebody (its length) increases whereas its bluntness (nose radius) decreases. To illustrate this, model F is selected from the Pareto front between E and A. The flowfield features of this model are illustrated in Fig. 23 whereas its design parameters and performance values are listed in Table 7.

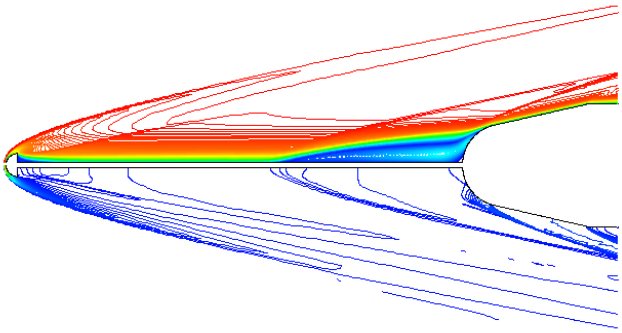

Figure 23 Features of the numerical flowfield of model F

Table 7 Design parameters and performance values for model F

Model	Design parameters						Drag coefficient		Peak heat flux, W/m^2	
	L'	r'	L'_s	r'_d	L'_d	r'_n	KG	CFD	KG	CFD
F	0.703	0.653	0.92	0.929	0.2	0.888	0.1968	0.223	6632.9	7398.3

The design of Model F is similar to that of model E. However, the forebody of the former is longer and its nose is less blunt. This causes the separation of the boundary layer to be closer to the forebody nose. Hence, the inclination of the effective body is higher compared with that of model E. consequently, the flow remains attached to the spike for a longer distance. These two factors explain the rise in drag in model F compared with model E. On the other hand, the shear layer reattachment on the forebody nose is stronger in model E. This can be clearly addressed by comparing the strength of the reattachment shocks in both models. As a consequence, the Aeroheating in model F is lower than that in model E. Model F can be viewed as an intermediate design between models A and E. Increasing the slenderness of the forebody and reducing its bluntness shift the optimal designs towards the minimum

aeroheating extreme, model A. Conversely, increasing the forebody bluntness and reducing its slenderness shift the designs towards lower drag and higher heating values.
On the other hand, as the optimal design evolves from model E towards models C and D, they can have different forms. Model G represents a typical optimal design in the Pareto front from E to C. Its flowfield features are illustrated in Fig. 26 and its design parameters and performance values are listed in Table 8.

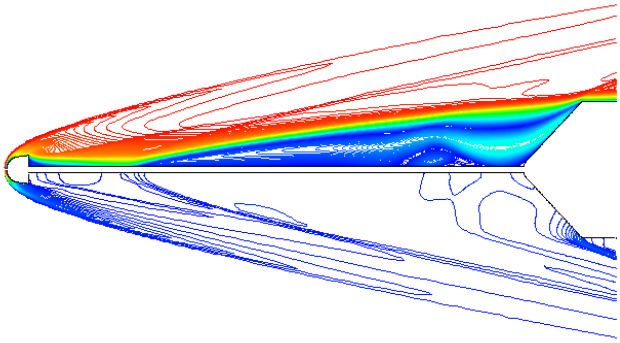

Figure 26 Features of the numerical flowfield of model G

Table 8 Design parameters and performance values for model G

Model	Design parameters						Drag coefficient		Peak heat flux, W/m^2	
	L'	r'	L'_s	r'_d	L'_d	r'_n	KG	CFD	KG	CFD
G	0.354	0.13	0.918	0.966	0.467	0.879	0.0842	0.0896	12953	12506

Model G has a different design compared with model E; its forebody is significantly shorter and less blunt. It can be assumed that further drag reduction by increasing the forebody nose bluntness may not yield optimal designs. Hence, different designs similar to model G appear on the Pareto front. Model G has the almost the same forebody face inclination as model D. The slightly higher drag of model G can be explained by the larger aerodisk base drag. The flow expansion at this area may be responsible for the drop in the downstream flow pressure. As a consequence, the flow separates earlier compared with model D. This may cause the shear layer reattachment to be smoother which explains the drop in peak heat flux value compared with model D.
As the optimal designs evolve towards model D, the forebody becomes more inclined with less blunt nose to enhance the early separation and yield more slender effective body (outlined by the shear layer). In addition, spikes can become slightly shorter to reduce the friction drag. However, highly inclined faces of the forebody can result in an unstable reattachment which yields unstable flowfield and hence unstable performance. The optimal models of such designs are situated towards model C on the unconstrained Pareto front. Inspired by Maull [3], we might expect that, adding a small roundness at the sharp corner of the forebody shoulder would encourage a more stable reattachment. The effect of such alternation on the optimality of these designs may invoke further investigation.

Conclusions

In the present study, the design of hypersonic spiked blunt bodies was optimized using the multi-objective NSGA-II algorithm coupled with Kriging surrogates. The objectives of optimization were minimizing both the drag and aerodynamic heating on the spiked body

whereas the flow stability was added as a constraint. The objectives and constraint functions surrogates were constructed using data from a high-fidelity Navier-Stokes CFD solver. The accuracy of the constructed surrogates was improved by eliminating some samples with undesired performance as well as adding more samples at the basins of the design space. It was shown that the aeroheating of the spiked model is mainly dictated by the forebody shape whereas the spike length mainly controls the drag response. The Pareto optimal set showed a degree of competition between the two design objectives. The optimized designs showed a considerable improvement in performance. In the absence of stability constraint, the model with minimum drag objective has a highly inclined forebody face which invokes unstable performance. By adding the stability constraint, the minimum attainable drag is slightly increased and the aeroheating objective is slightly affected. For both objectives with and without the constraint, a long spike is preferred.

References

[1] Jagadeesh, G., Viren, M., Reddy, K. P. J., Hashimoto, T., Sun, M., and Takayama, K., "Hypersonic Buzz Phenomenon in the Spiked Blunt Cones," AIAA paper 2003-284, 2003

[2] Shoemaker, J. M., "Aerodynamic Spike Flowfields Computed to Select Optimum Configuration at Mach 2.5 with Experimental Validation," AIAA paper 90-0414, 1990.

[3] White, J. T., "Application of Navier-Stokes Flowfield Analysis to the Aerothermodynamic Design of an Aerospike-Configured Missile," AlAA paper 93-0968, 1993

[4] Gnemmi, P., Srulijes, J. and Roussel, K., "Flowfield around Spike-Tipped Bodies for High Attack Angles at Mach 4.5," *Journal of Spacecraft and Rockets*, Vol. 40, No. 5, 2003, pp. 622- 631

[5] Mehta, R. C., "Numerical Heat Transfer Study over Spiked Blunt Bodies at Mach 6.8," *Journal of Spacecraft and Rockets*, Vol. 37, No. 5, 2000, pp. 700- 703

[6] Heubner, L. D. Mitchell, A. M. and Boudreaux, E. J., "Experimental Results on the Feasibility of an Aerospike for Hypersonic Missiles", *AIAA paper*, 95-0737, Jan.1995.

[7] Mehta, R. C., "Peak Heating for Reattachment of Separated Flow on a Spiked Blunt Body," *Heat and Mass Transfer*, Vol. 36, 2000, pp. 277- 283

[8] Wagner, R. D. and Pine, C. P., "Laminar Heat Transfer and Pressure Distribution Studies on a Series on Re-Entry Nose Shapes at a Mach Number of 19.4 in Helium," NASA TN D-891, 1961

[9] Maull,D. J. "Hypersonic Flow over Axially Symmetric Spiked Bodies," *Journal of Fluid Mechanics*, Vol. 8, P.4, 1960, pp. 584-592

[10] Menezes, V., Saravanan, S., Jagadeesh, G., and Reddy, K. P. J., "Experimental Investigations of Hypersonic Flow over Highly Blunted Cones with Aerospikes," AIAA Journal, Vol. 41, No. 10, 2003, pp. 1955- 1966

[11] Bogdonoff , S. M. and Vas , I. E., "Preliminary Investigations of Spiked Bodies at Hypersonic Speeds," *Journal of the Aerospace Sciences*, Vol. 26, No. 2, 1959, pp. 65-74

[12] Alexander, S. R., "Results of Tests to Determine the Effect of a Conical Windshield on the Drag of a Bluff Body at Supersonic Speeds," NACA RM L6K08a, January, 1947.

[13] Jones, J. J., "Flow Separation from Rods Ahead of Blunt Noses at Mach Number 2.7," NACA RM L52E05a, July, 1952

[14] Gauer, M. and Paull, A., "Numerical Investigation of a Spiked Blunt Nose Cone at Hypersonic Speeds," Journal of Spacecraft and Rockets, Vol. 45, No. 3, 2008, pp. 459 -471

[15] Reding, J. P., Guenther, R. A., and Richter, B. J., "Unsteady Aerodynamic Considerations in the Design of a Drag-Reduction Spike," *Journal of Spacecraft and Rockets*, Vol. 14, No. 1, 1977, pp. 54- 60

[16] Mehta, R. C., "Flow Field Computations Over Conical, Disc and Flat Spiked Body at Mach 6", AIAA paper 2009-325, 2009

[17] Kalimuthu, R., Mehta, R. C., and Rathakrishnan, E., "Experimental Investigation on Spiked Body in Hypersonic Flow," *The Aeronautical Journal*, Vol. 112, No. 1136, 2008, pp. 593- 598

[18] Panaras, A. G. and Drikakis, D., "High-Speed Unsteady Flows around Spiked-Blunt Bodies," Journal of Fluid Mechanics, Vol. 632, 2009, pp. 69-96

[19] Guenther, R. A. and Reding, J. P., "Fluctuating Pressure Environment of a Drag Reduction Spike," Journal of Spacecraft and Rockets, Vol. 14, No. 12, 1977, pp. 705 - 710

[20] Motoyama, N., Mihara, K., Miyajima, R., Watanuki, T., and Kubota, H., "Thermal Protection and Drag Reduction with Use of Spike in Hypersonic Flow," AIAA paper 2001-1828, 2001

[21] Crawford, D. H. "Investigation of The Flow over a Spiked-Nose Hemisphere-Cylinder," NASA TN-D-118, Dec.1959

[22] Album, H. H., "Regarding the Utility of Spiked Blunt Bodies," Journal of the Aerospace Sciences, Vol. 5, No. 1, 1968, pp. 112- 113

[23] Calarese, W. and Hankey, W., "Modes of Shock-Wave Oscillations on Spike-Tipped Bodies," AIAA Journal, Vol. 23, No. 2, 1985, pp. 185-192.

[24] Kurbatskii K. A. and Montanari, F., "Application of Pressure-Based Coupled Solver to the Problem of Hypersonic Missiles with Aerospikes," AIAA paper 2007-462, 2007.

[25] Milicev, S. S. and Pavlovic, M. D., "Influence of Spike Shape at Supersonic Flow Past Blunt-Nosed Bodies: Experimental Study," *AIAA Journal*, Vol. 40, No. 5, 2001, pp. 1018- 1020

[26] Beastall, D. and Turner, J., "The Effect of a Spike Protruding in Front of a Bluff: Body at Supersonic Speeds," Aeronautical Research Council, R. & M. No. 3007, 1957

[27] Holden, M., "Experimental Studies of Separated Flows at Hypersonic Speeds. Part I-Separated Flows over Axisymmetric Spiked Bodies," *AIAA Journal*, Vol. 4, No. 4, 1966, pp. 591-599

[28] Antonov, A. N., and Grestov, V. K., "Unsteady Separated Supersonic Flow over Pointed and Spiked Bodies," Fluid Dynamics, Vol. 9, No. 4,1974.pp. 578- 582.

[29] Stalder, J. R. and Nielson, H. V., "Heat Transfer from a Hemisphere Cylinder Equipped with Flow Separation Spikes," NACA TN 3287, Sept. 1954.

[30] Moeckel, W. E., " Flow Separation Ahead of a Blunt Axially Symmetric Body at Mach Numbers 1.76 to 2.10," NACA RM E51I25, 1951

[31] Hermach, C. A., Kraus, K., and Reller, J. O., " Reduction in Temperature-Recovery Factor Associated with Pulsating Flows Generated by Spike-Nosed Cylinders at a Mach Number of 3.50," NACA RM A56L05, March, 1957.

[32] Jones, J. J., "Experimental Drag Coefficients of Round Noses with Conical Windshields at Mach Number 2.72," NACA RM L55E10, June, 1955.

[33] Ahmed, M. and Qin, N., "Drag Reduction Using Aerodisks for Hypersonic Hemispherical Bodies," Journal of Spacecraft and Rockets, Vol. 47, No. 1, 2010, pp. 62-80.

[34] Jagadeesh, G., Viren, M., Reddy, K. P. J., Hashimoto, T., Sun, M., and Takayama, K., "Hypersonic Buzz Phenomenon in the Spiked Blunt Cones," AIAA paper 2003-284, 2003

[35] Ahmed, M. and Qin, N., "Metamodels for aerothermodynamic design optimization of hypersonic spiked blunt bodies," Aerospace Science and Technology, Vol. 14, Issue 5, 2010, pp. 364- 376.

[36] Karlovskii, V. N. and Sakharov, V. I., "Numerical Investigation of Supersonic Flow past Blunt Bodies with Protruding Spikes," *Fluid Dynamics, Vol. 21, No., 3, 1986, pp. 437- 445*

[37] Antonov, A. N., Gretsov, V. K. and Shalaev, S. P., "Nonsteady Supersonic Flow over Spiked Bodies," Fluid Dynamics, Volume 11, Number 5 / September, 1976, pp. 746-751

[38] Hur, K. H., Kirn, S .T. and Lee, D. H., " Numerical Analysis on Supersonic, Viscous Flowfield around a Spike-Nosed Projectile with Fins," AIAA paper 96-3449-CP, 1996

[39] McGhee, R. J. and Staylor, W. F.," Aerodynamic Investigation of Sharp Cone-Cylinder Spikes on 120^{o} Blunted Cones at Mach Numbers of 3, 4.5, and 6," NASA TN D-5201, 1969

[40] McKay, M. D., Beckman, R. J., Conover, W. J., "A Comparison of Three Methods for Selecting Values of Input Variables in the Analysis of Output from a Computer Code," Technometrics, Vol. 21, No. 2, 1979, pp. 239-245

[41] Morris, M. D. and Mitchell, T. J. "Exploratory Designs for Computational Experiments," Journal of Statistical Planning and Inference, Vol. 43, 1995, pp.381-402

[42] Viana, F. A. C., "SURROGATES Toolbox User's Guide," http://fchegury.googlepages.com, Cited, Dec. 2009.

[43] "U.S. Standard Atmosphere, 1976," NASA – TM – X- 74335, 1976.

[44] Fluent 6.3 User Guide, Fluent Inc., Lebanon, NH 03766 , USA

[45] Gambit 2.4 User Guide, Fluent Inc., Lebanon, NH 03766 , USA

[46] D. G. Krige, "A study of gold and uranium distribution patterns in the Klerksdorp gold field," Geoexploration, Vol. 4, No. 1, 1966, pp. 43–53.

[47] Matheron, G., "Principles of Geostatistics," Economic Geology,Vol. 58, 1963, pp. 1246–1266

[48] Sacks, J., Welch, W. J., Mitchell, T. J., and Wynn, H. P., "Design and Analysis of Computer Experiments," Statistical Science, Vol. 4, No. 4, 1989, pp. 409-423

[49] Lim, Y. B., Sacks, J., Studden, W. J., and Welch, W. J., "Design and Analysis of Computer Experiments when the Output is Highly Correlated Over the Input Space," National Institute of Statistical Sciences Technical Report Number 62, 1997

[50] Queipo, N. V., Haftka, R. T., Shyy, W., Goel, T., Vaidyanathan, R., and Tucker, K., "Surrogate-based Analysis and Optimization," Progress in Aerospace Sciences, Vol. 41, 2005, pp. 1-28

[51] Jin, R., Chin, W., and Simpson, T. W., "Comparative Studies of Metamodeling Techniques under Multiple Modeling Criteria," *AIAA Paper 2000-4801*, 2000.

[52] Martin , J. D. and Simpson, T. W., "Use of Kriging Models to Approximate Deterministic Computer Models," AIAA Journal, Vol. 43, No. 4, 2005, pp. 853-863

[53] Laurenceau, J. and Sagaut, P., "Building Efficient Response Surfaces of Aerodynamic Functions with Kriging and Cokriging," AIAA Journal, Vol. 46, No. 2, 2008, pp. 498-507

[54] Jeong, S., Murayama, M., and Yamamoto, K., "Efficient Optimization Design Method Using Kriging Model," Journal of Aircraft, Vol. 42, No. 2, 2005, pp. 413-420

[55] Kampolis, I. C. and Giannakoglou, K. C., "A Multilevel Approach to Single- and Multiobjective Aerodynamic Optimization," Computer Methods in Applied Mechanics and Engineering, Vol. 197, 2008, pp. 2963–2975

[56] Deb, K., Pratap, A., Agarwal, S., and Meyarivan, T., “A fast and elitist multiobjective genetic algorithm: NSGA-II,” IEEE Transactions on Evolutionary Computation, Vol. 6, No.2, 2002, pp. 182–197

[57] NSGA-II toolbox for Matlab user guide, http://www.mathworks.com/matlabcentral/fileexchange/10429-nsga-ii-a-multi-objective-optimization-algorithm, cited Jan 2010

[58] Zitzler, E., Deb, K., and Thiele, L., „Comparion of Multiobjective Evolutionary Algorithms: Empirical Results,“ Evolutionary Computation, Vol. 8, No.2, 2000, pp. 173-195

[59] Konak, A.,Coit, D. W., and Smith, A. E., "Multi-objective Optimization Using Genetic Algorithms: A tutorial," Reliability Engineering and System Safety, Vol. 91, 2006, pp. 992-1007

[60] Matlab 7 release 14 User Guide, The Mathworks Inc., USA

[61] Chapman, D. R., Kuehn, D. M., and Larson, H. K., "Investigation of Separated Flows in Supersonic and Subsonic Streams with Emphasis on the Effect of Transition," NACA TR 1356, 1957

[62] Wood, C. J., “Hypersonic Flow over Spiked Cones,” Journal of Fluid Mechanics, Vol. 12, Pt. 4, 1961, pp. 614–624.

[63] Keane, A. J., " Wing Optimization Using Design of Experiment, Response Surface, and Data Fusion Methods," AIAA Journal, Vol. 40, No. 4, 2003, pp. 471-450

[64] Sobol, I. M., “Global Sensitivity Indices for Nonlinear Mathematical Models and Their Monte Carlo Estimates,” Mathematics and Computers in Simulation, Vol. 55, 2001, pp. 271-280